Article

Poly(vinyl alcohol) Embedded with Montmorillonite Clay and Nano Titania: A Scale-Up for Sustainable Environmental Remediation

Bindu Mavila,*,[§] Hareesh Pradeep,[§] Shwetha Suresh,[§] Najiya Cheroor Konathodi, Anil Adukkadan, Monika Monika, and Pradeepan Periyat*

Read Online

ACCESS | Metrics & More | Article Recommendations | Supporting Information

ABSTRACT: A poly(vinyl alcohol)/montmorillonite/titania (PVA/MMT/TiO$_2$) nanocomposite film was fabricated via a simple solution casting strategy for the removal of cationic as well as anionic dyes. The developed nanocomposite film was subjected to X-ray diffraction (XRD), Fourier transform Infrared (FTIR), thermogravimetric analysis, dynamic mechanical analysis (DMA), mechanical property evaluation, and scanning electron microscopy (SEM) analysis. The embedding of MMT and TiO$_2$ nanoparticles onto a PVA matrix has been confirmed from XRD, FTIR, and SEM analysis. It has been found that the thermal and mechanical properties of virgin PVA have been significantly improved by embedding it with MMT and TiO$_2$. The embedded system also exhibited excellent room-temperature storage modulus compared to the unfilled system, as revealed from DMA. By utilizing the adsorption characteristics of MMT and photocatalytic activity of TiO$_2$, the developed PVA/MMT/TiO$_2$ nanocomposite film was used for the removal of model dyes, viz, malachite green (MG), methylene blue (MB), and cotton blue (CB). The highest removal efficiency for cationic MG and MB was 99.99% and 99.79%, respectively, for 15 min of exposure time. The anionic CB showed a removal efficiency of 98.52%. The highlight of the work is that, since the adsorbent and photocatalyst are embedded onto a polymer matrix and made in the form of a film, we can easily recover the film from the solution after use, with no need of centrifugation and further purification strategies as in the case of powderous photocatalysts. Further, the PVA/MMT/TiO$_2$ nanocomposite film exhibited excellent reusability of 10 cycles, which is a very high value in comparison with literature reports.
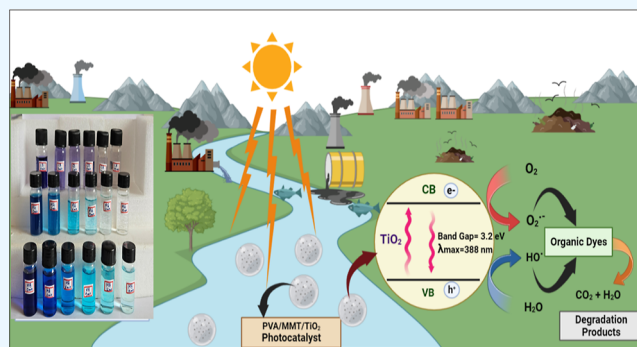
INTRODUCTION

The usage of a broad range of coloring pigments and dyes has seen a surge in demand in the textile, leather, food, paint, pharmaceutical, and medical diagnostic industries as a result of fast urbanization, rapid economic expansion, and industrialization.[1,2] However, the effluents that are discharged from these industries have a negative effect on the environment since they are improperly treated before being put into sewage and eventually end up in adjacent water bodies such as rivers, lakes, and streams. These discharges may contain heavy metals, inorganic salts, carcinogenic compounds, and colors that not only harm the environment but also contaminate drinking water sources.[3,4] Dyeing chemicals possess aromatic backbones with a stable structure and are resistant to oxidizing agents, light, and heat; further, they are not biodegradable and stay in the water for years, which is another important worry.[5] However, certain colors break down into more dangerous substances that endanger the ecosystem. For instance, the largest class of synthetic dyes is synthetic nitrogen dyes, also known as azo dyes, which under specific circumstances degrade and emit carcinogenic aromatic amines.[6] These toxic compounds cause cancer,

kidney, and liver damage, neurological disorders, and other diseases in humans when they are exposed to them.[7] As a result, it is now a worldwide priority to discover a sustainable method for the effective removal of organic dyes from contaminated water.

Adsorption and coagulation strategies are the traditional methods of dye removal, and have been found to be less effective because the solid materials that are adsorbed or coagulated on the adsorbent surface require further processing.[8−10] Photocatalysis has been reported to be a promising tool to resolve these issues. It employs an advanced oxidation process, which has a high level of efficiency in treating wastewater that contains chemical contaminants.[11] Among the semiconductor nanoparticles, nano titania (TiO$_2$) has received the most attention as
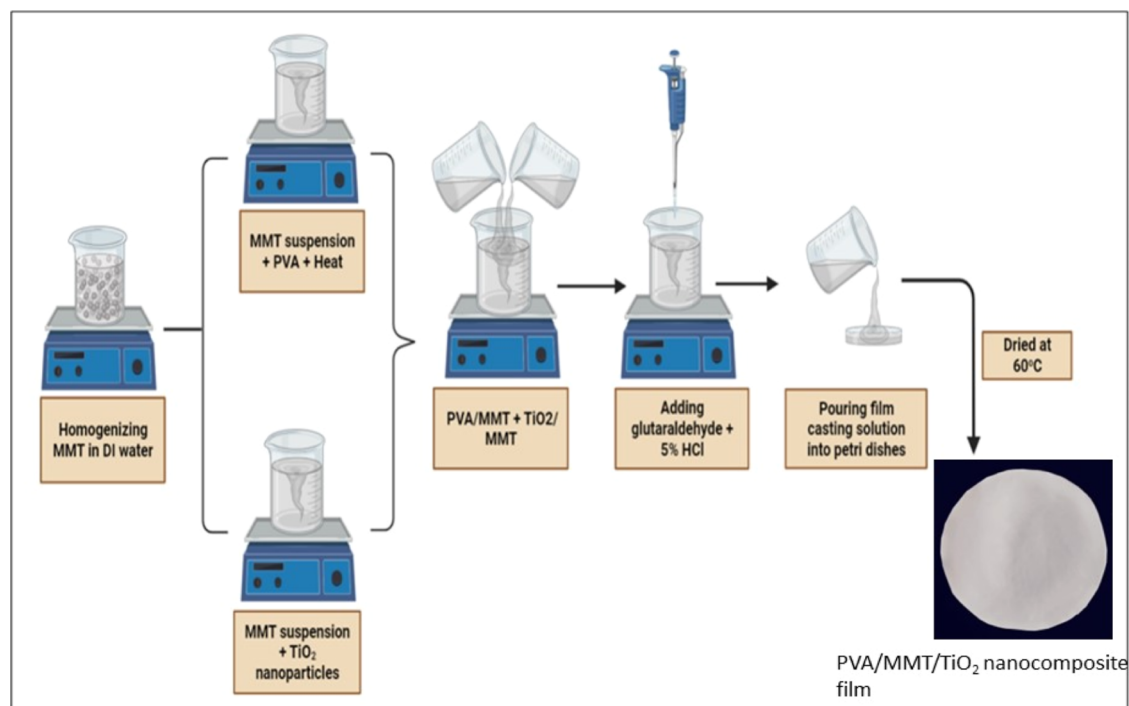
Figure 1. Schematic representation of the development of the PVA/MMT/TiO$_2$ nanocomposite film.

an effective photocatalyst.[12,13] Even though TiO$_2$ nanoparticles are having impressive photocatalytic activity, their use is constrained by a number of issues, including inadequate solar energy absorption, challenges with recycling, high rate of photogenerated electron hole recombination, and agglomeration.[14−16] Traditional sedimentation or centrifugal isolation techniques are required to recover the photocatalyst after the water treatment.[17] The process is energy consuming and also leads to secondary pollution to the environment, restricting the applications of the TiO$_2$ photocatalyst for water treatment application.

Studies have been carried out to incorporate TiO$_2$ nanoparticles onto various substrates such as silica, graphene oxide, carbon nitride, activated carbon, etc., in view of possible enhancement in the functional properties of TiO$_2$.[18−21] However, these opaque substances cause a reduction in the light utilization efficiency and decrease the performance of the photocatalyst. Literature reports reveal that polyhydroxylated compounds improve the photocatalytic activity of TiO$_2$.[22,23] It has been observed that the capacity of glucose to scavenge holes increases the photoactivity of TiO$_2$.[24,25] However, to use the TiO$_2$/glucose system as a stable photocatalyst, the photo-degradation of tiny glucose molecules posed a significant challenge. It was therefore solely employed as a hole scavenger. As a stable matrix for the TiO$_2$ photocatalyst, the polyhydroxy-lated polymer, poly(vinyl alcohol) (PVA) is a more promising candidate.[26,27] PVA is a nontoxic, hydrophilic polymer which has excellent film-forming ability, high chemical and thermal stability, environmental friendliness, water solubility, gas solubility,[28−33] flexibility, and transparency.[34,35] More crucially, the PVA chain's abundance of −OH groups significantly improves its ability to scavenge the holes. As a result, PVA can be chosen as a useful support for incorporating TiO$_2$ in order to build a photoreduction system based on effective holes scavenging.

Montmorillonite clay (MMT) has been reported to be very efficient in reinforcing polymer matrices and thereby improves the mechanical properties.[36,37] MMT composed of one Al^{3+} octahedra connected with two Si^{4+} tetrahedra shows excellent adsorption characteristics owing to the surface charge and hydrophilicity.[38−41] MMT can interact with hydrophilic polymers due to its inherent chemical makeup, which include the presence of silanol groups (−Si−OH) on the surface and its capacity to create hydrogen bonds.[42] MMT can therefore function as cocross-linkers of hydrophilic polymers in solution and contribute enhanced stability to the nanocomposite.

In the present study, we report the development of PVA/MMT/TiO$_2$ nanocomposite films via a simple solvent casting strategy, for the efficient removal of both cationic dyes (malachite green; MG and methylene blue; MB) and anionic dyes (cotton blue; CB). The dye removal efficiency has been investigated in terms of nanocomposite dosage, TiO$_2$ loading, MMT loading, pH, contact time, initial dye concentration, and temperature. Reusability of the PVA/MMT/TiO$_2$ nanocomposite film was also examined. The mechanism of dye removal involves both adsorption and photocatalysis. Detailed investigations on isotherm, kinetics, and thermodynamics of adsorption have been carried out. The Langmuir adsorption isotherm model has been found to be the best fit with experimental data and the dye adsorption follows pseudo-second-order kinetics. The spontaneity and hence the feasibility of dye adsorption has been confirmed from thermodynamic investigations.

■ EXPERIMENTAL SECTION

Materials and Methods. PVA (99%, molecular weight: 89,000−98,000; Sigma-Aldrich, USA), montmorillonite K10 (MMT; Thermo Fisher Scientific India Pvt. Ltd. Mumbai, India), glutaraldehyde (25% in water, Spectrochem. Ltd., Mumbai, India), titanium isopropoxide (Thermo Fisher Scientific India Pvt. Ltd. Mumbai, India), and glacial acetic

acid (Spectrochem. Ltd., Mumbai, India) were all of analytical grade and used directly without further purification. The model dyes used in this study, viz, MG and MB, were purchased from Sigma-Aldrich, USA and CB from Spectrum Chemicals Pvt. Ltd., Mumbai, India. Deionized water was used as the solvent for the development of the nanocomposite film and also for the dye removal studies.

Development of PVA/MMT/TiO$_2$ Nanocomposite Films. TiO$_2$ nanoparticles were synthesized initially via a modified method as reported earlier.[43] Titanium isopropoxide, glacial acetic acid, and deionized water were used as precursors for the synthesis of TiO$_2$ nanoparticles. Glacial acetic acid (71.5 mL) was added to titanium isopropoxide (36 mL) under constant stirring. Then, a definite volume of deionized water (225 mL) was added to this mixture and the stirring continued. A stable sol was formed, which could be converted into gel form by heating in a water bath at 100 °C for 12 h. The dried powder was then calcined at 600 °C to obtain the TiO$_2$ nanoparticles. Titanium isopropoxide hydrolyzes vigorously with water, to form a white titanium hydroxide precipitate. By the addition of glacial acetic acid, the rate of hydrolysis decreases and titanium hydroxide particles get dispersed to form a stable sol.

The PVA/MMT/TiO$_2$ nanocomposite films were fabricated via a simple solution casting strategy. A schematic representation of the development of PVA/MMT/TiO$_2$ nanocomposite films has been depicted as Figure 1. Initially, MMT was added to deionized water and was sonicated for 2 h to disperse MMT. The MMT dispersion was then divided into two equal portions; to the first portion, PVA was added and heated with stirring (at 90 °C) to dissolve PVA completely. To the second portion of MMT dispersion, TiO$_2$ nanoparticles (average particle size-20 nm) were added and sonicated for 2 h. The first portion now contains PVA solution with dispersed MMT and the second portion contains a dispersion of MMT and TiO$_2$. Both these portions were mixed together to obtain a film-forming solution of PVA/MMT/TiO$_2$ and was stirred for 1 h to ensure proper mixing. This was followed by the addition of cross-linking agent glutaraldehyde/HCl (0.2 mL glutaraldehyde/0.15 mL 5% HCl) and the stirring continued overnight at room temperature. The film-forming solutions were then poured into a Petridish and dried at 60 °C for 24 h to obtain PVA/MMT/TiO$_2$ nanocomposite films of average thickness of 0.2 mm.

Altogether, 16 compositions of nanocomposite films were prepared by varying the amount of MMT and TiO$_2$ as shown in Table 1 (composition of PVA was kept constant).

Characterization Techniques. A Panalytical Empyrean X-ray diffractometer was used to record the X-ray diffractograms of the developed PVA/MMT/TiO$_2$ nanocomposite film (operating at 40 kV, 30 mA), using Cu Kα radiation ($\lambda = 1.5405$ Å) with a position sensitive detector. Diffraction data were collected in the range 0−90°. Fourier transform infrared (FTIR) spectra of the samples were obtained in ATR mode by using JASCO FTIR-4700, in the wavenumber range of 400−4000 cm^{-1}. Thermal analysis was performed with a thermogravimetric analysis instrument (TA Instruments, Q50). The thermogravimetric analysis (TGA) data were recorded from room temperature to 600 °C at a scan rate of 10 °C/min. Morphology of the system was evaluated by scanning electron microscopy (SEM) (Hitachi-2400). Mechanical properties of the nanocomposite films were examined by using a universal testing machine (Shimadzu Autograph, AG-Xplus series) with an applied load of 10 N. Dynamic mechanical analysis (DMA) was performed by using a viscoelastometer (DMTA, model no: MK-II) in the

Table 1. Sample Formulations

no.	PVA (wt %)	MMT (wt %)	TiO$_2$ (wt %)
1	3	0.025	0.20
2	3	0.025	0.30
3	3	0.025	0.40
4	3	0.025	0.50
5	3	0.050	0.20
6	3	0.050	0.30
7	3	0.050	0.40
8	3	0.050	0.50
9	3	0.075	0.20
10	3	0.075	0.30
11	3	0.075	0.40
12	3	0.075	0.50
13	3	0.100	0.20
14	3	0.100	0.30
15	3	0.100	0.40
16	3	0.100	0.50

temperature range of room temperature to 150 °C at a 10 Hz frequency. The test specimens were 55 mm in length, 5 mm in width, and 2 mm in thickness. The dye removal studies were investigated by using a UV−visible spectrophotometer, UV-2700, Shimadzu, Japan.

Swelling and Solubility Studies. Swelling studies give interesting information regarding the interfacial strength and dispersion of the filler in the polymer matrix. For evaluating the degree of water uptake, the preweighed nanocomposite film was immersed in distilled water (100 mL) and allowed to soak for 24 h at room temperature to attain equilibria. After the samples were removed from water, the film was blotted with filter paper and weighed to obtain the weight of the swollen sample. Finally, the swelling percentage was calculated by using the expression[44,45]

$$\text{degree of swelling (\%)} = \frac{W_2 - W_1}{W_1} \cdot 100 \tag{1}$$

where W_1 (g) and W_2 (g) are the weight of the dried and swollen samples, respectively.

Dye Removal Studies. Dye removal studies were conducted by treating a preweighed quantity of PVA/MMT/TiO$_2$ nanocomposite film with 100 mL of dye solutions containing different concentrations of the dye. The solution was first kept in a dark chamber to allow the system to reach adsorption−desorption equilibrium. Then, the solution with the catalyst was exposed to direct sunlight and stirred with a uniform agitation speed of 500 rpm. 5 mL of the sample solution was collected from the system at a definite interval of time and was analyzed with a UV−visible spectrophotometer to find the absorbance and hence the dye concentration. The percentage removal efficiency (R %) was calculated by using the following equation.[46,47]

$$R \% = \frac{C_0 - C_e}{C_0} \cdot 100 \tag{2}$$

The amount of dye adsorbed per unit mass of nanocomposite film (q_e) was calculated by using the expression.[48]

$$q_e = \frac{(C_0 - C_e) \times V}{W} \tag{3}$$

where C_o and C_e (mg/L) are the concentrations of dye solution before and after adsorption, respectively, V is the volume of the dye solution (in liter), and W is the weight of the nanocomposite film (g).

Reusability. To examine the reusability of the developed PVA/MMT/TiO$_2$ nanocomposite film, the film after optimized conditions of dye removal, was dipped in a 0.1 M HCl solution for 3 h. The film was then taken out, washed, air-dried, and was used for the next cycle test.[49] The reusability was investigated in ten consecutive cycles, under identical experimental conditions.

■ RESULTS AND DISCUSSION

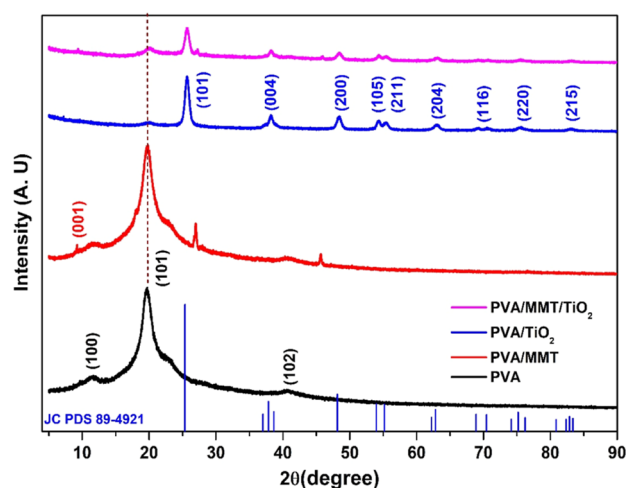Figure 2 shows the X-ray diffraction (XRD) pattern of PVA, PVA/MMT, PVA/TiO$_2$, and PVA/MMT/TiO$_2$ systems. PVA

Figure 2. XRD pattern of PVA, PVA/MMT, PVA/TiO$_2$, and PVA/MMT/TiO$_2$ systems.
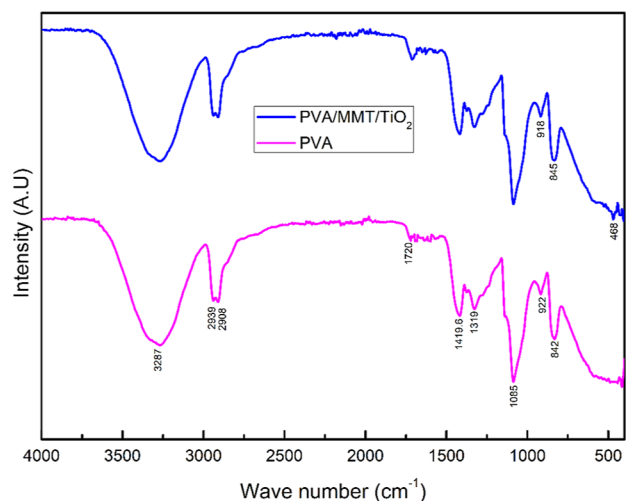

Figure 3. FTIR spectra of PVA and PVA/MMT/TiO$_2$ systems.

is a semicrystalline polymer and diffraction peaks were observed at $2\theta = 11.55$, 19.70 and 40.74°, owing to the diffraction from (100), (101), and (102) planes, respectively.[50] In the case of the PVA/MMT system, the peaks at $2\theta = 9.1°$ correspond to the basal spacing or (001) diffractions of MMT and those at 45.0° are due to clay impurities.[51] For the PVA/TiO$_2$ system, in addition to the diffraction peaks of PVA, diffraction peaks were identified at 25.74, 38.16, 48.28, 54.40, 55.35, 62.96, 69.24,

70.42, 75.47, and 82.71° corresponding to the diffraction from TiO$_2$ planes (101), (004), (200), (105), (211), (204), (116), (220), (215), and (303), respectively. This indicates that the crystallinity of TiO$_2$ does not change during nanocomposite formation. These results are in agreement with JCPDS no. 89-4921. In the case of the PVA/MMT/TiO$_2$ system, both the diffraction peaks of PVA/MMT and PVA/TiO$_2$ were seen. However, the most intense peak of PVA at 19.7° was significantly less intense and broadened.

FTIR spectra of PVA and PVA/MMT/TiO$_2$ systems have been shown as Figure 3. For virgin PVA, the −OH stretching vibrations from intermolecular and intramolecular hydrogen bonds were observed at 3287 cm^{-1}. The peaks at 2908 and 2939 cm^{-1} correspond to the C−H vibrations from aldehyde. The −C═O and −CH$_2$ vibrations have been observed at 1720 and 1419 cm^{-1}, respectively. The peaks at 1319 cm^{-1} correspond to CH−OH bending and CH$_2$ wagging and those observed at 1085 cm^{-1} indicate C−O stretching vibrations. −CH$_2$ rocking vibrations have been observed at 922 cm^{-1} and C−C stretching vibrations at 842 cm^{-1}.[52] In the case of PVA/MMT/TiO$_2$ systems, the peaks at 918 and 845 cm^{-1} correspond to Al−O stretching vibrations and those at 468 cm^{-1} arise due to Si−O bending vibrations.[53] Ti−O stretching vibrations were also observed at 468 cm^{-1}.[54] Figure 4 shows possible interactions among the constituents of the nanocomposite.

Mechanical Properties. Since the developed PVA/TiO$_2$/MMT films have been employed for dye polluted water treatment, evaluation of their mechanical properties is very crucial. The mechanical properties such as tensile strength, Young's modulus, and elongation at break of PVA, PVA/TiO$_2$, PVA/MMT, and PVA/TiO$_2$/MMT systems have been examined and the results are presented in Table 2. We have evaluated the effect of nano TiO$_2$ and MMT content on the mechanical properties of PVA/MMT and PVA/TiO$_2$ systems, respectively. It has been observed that PVA/TiO$_2$/MMT systems exhibited improved mechanical properties than virgin PVA and their binary systems, i.e., PVA/TiO$_2$ and PVA/MMT systems. As the MMT content reaches 0.1%, the tensile strength and Young's modulus increased by 66% and 86%, respectively. The MMT provides extensive surface area for creating number of interactions among PVA and MMT, restricting the segmental mobility, acting as mechanical reinforcement at the expense of flexibility. The interaction among the constituents has been proved from FTIR analysis. The addition of TiO$_2$ had a dual influence on the mechanical properties. The loading of 0.4% TiO$_2$ led to an increment in tensile strength and Young's modulus by 42% and 54%, respectively. However, when it reaches 0.5%, the tensile strength and Young's modulus have been decreased.

The reinforcing effect of TiO$_2$, which caused an increase in the values of both tensile strength and modulus, is due to the interaction among PVA and TiO$_2$ nanoparticles. When the TiO$_2$ content reaches 0.5%, mechanical properties are weakened, possibly due to the formation of agglomerates, which in turn creates weak regions in the matrix. Similar observations have been reported for the influence of higher loading of nanoparticles such as TiO$_2$, ZnO, etc. on the mechanical properties of different types of polymer matrices.[55,56] It has been observed that both MMT and TiO$_2$ incorporation decrease the elongation at break values. The reduction in elongation at break indicates that the incorporation of nanoparticles restricted the motion of PVA chains owing to the strong interaction among the constituents.
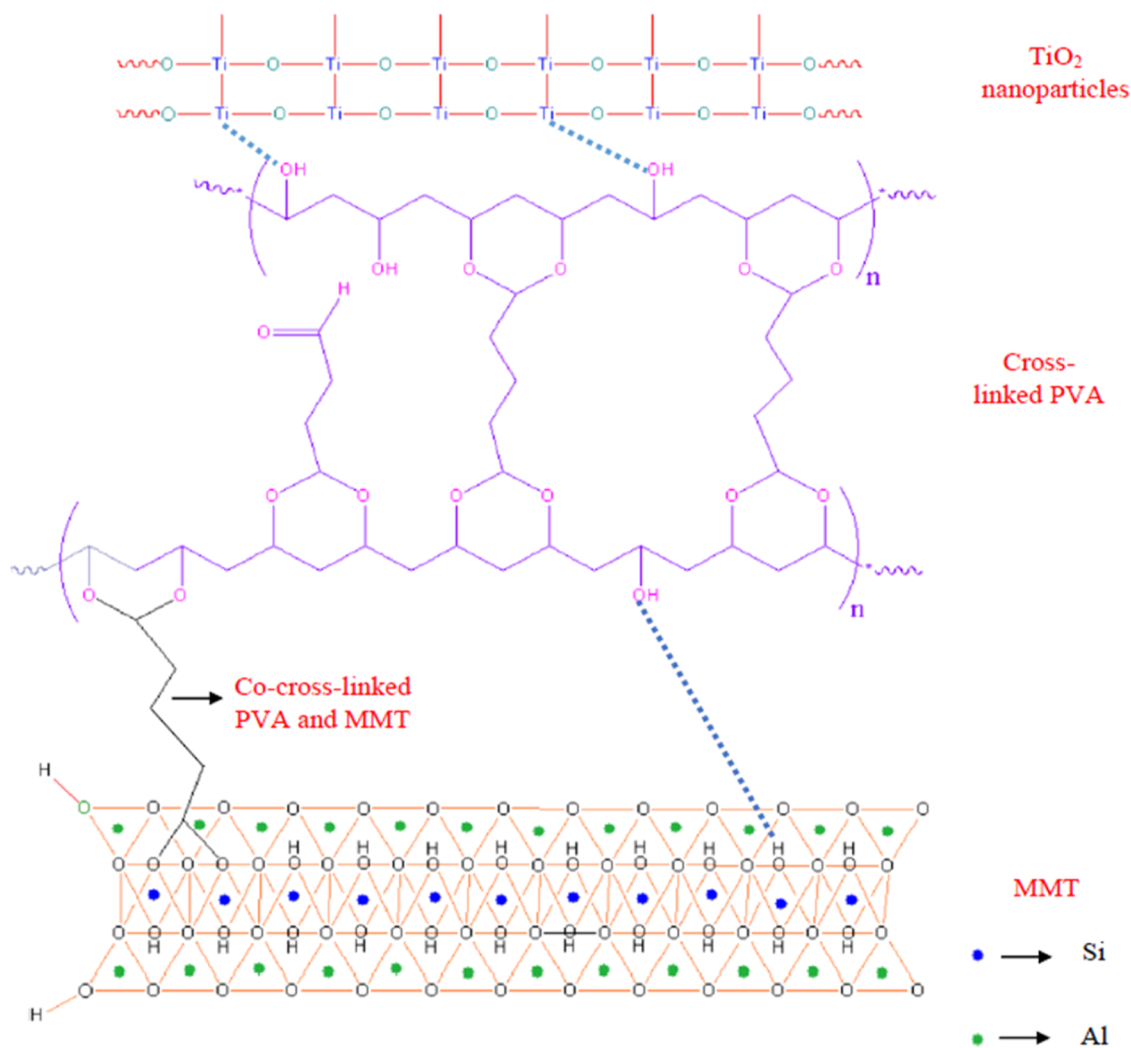
Figure 4. Possible interactions among the constituents of the PVA/MMT/TiO$_2$ system.

Table 2. Mechanical Properties of PVA, PVA/TiO$_2$, PVA/MMT, and PVA/TiO$_2$/MMT Systems

samples	tensile strength (MPa)	Young's modulus (MPa)	elongation at break (%)
PVA	39.23 ± 1.89	8.95 ± 0.56	291.30 ± 3.83
PVA/TiO$_2$	44.93 ± 1.58	11.42 ± 0.84	272.51 ± 4.53
PVA/MMT	46.83 ± 1.09	9.88 ± 0.53	270.14 ± 3.92
PVA/MMT/TiO$_2$-0.2%	47.95 ± 1.93	11.63 ± 0.72	261.23 ± 3.05
PVA/MMT/TiO$_2$-0.3%	51.09 ± 2.53	12.86 ± 0.63	250.64 ± 4.29
PVA/MMT/TiO$_2$-0.4%	55.87 ± 2.98	13.82 ± 0.45	242.43 ± 3.23
PVA/MMT/TiO$_2$-0.5%	49.69 ± 1.99	12.09 ± 0.76	241.58 ± 3.74
PVA/MMT-0.025%/TiO$_2$	48.98 ± 2.96	13.36 ± 0.94	262.34 ± 4.21
PVA/MMT-0.050%/TiO$_2$	49.69 ± 2.84	14.82 ± 0.68	254.73 ± 4.18
PVA/MMT-0.075%/TiO$_2$	56.37 ± 2.06	15.28 ± 0.81	246.30 ± 3.95
PVA/MMT-0.10%/TiO$_2$	65.13 ± 1.64	16.73 ± 0.27	239.85 ± 3.06

Dynamic Mechanical Analysis. DMA has been carried to investigate the influence of nanofiller embedding on the storage modulus and loss factor of PVA. The variation of storage modulus (E') versus temperature for PVA, PVA/MMT, and PVA/MMT/TiO$_2$ nanocomposite films have been shown as Figure 5a. For all the systems, the storage modulus decreases steadily with an increase in temperature and attains a limiting value after a particular temperature. This has been attributed to the increased segmental mobility and thereby increased free volume between the segments with respect to the temperature. It has been found that the storage modulus of neat PVA and PVA/MMT system is lower than the PVA/MMT/TiO$_2$ system for all the temperatures. This is a clear indication of the effective reinforcement of the PVA matrix by MMT and TiO$_2$ nanoparticles, owing to which the segmental motion gets restricted. We have further investigated the effect of MMT loading on the storage modulus of the nanocomposite, and the results have been presented as Figure 5c. As the MMT loading increases from 0.025 to 0.1 wt %, the storage modulus increases by 7%. This improvement has been attributed to the significant reinforcement offered by MMT particles. Owing to the large surface area and van der Waals force of attraction with the PVA matrix, MMT restricts the segmental mobility and deformability of PVA matrix.

Figure 5b shows the loss factor (tan δ) and the ratio of loss modulus to storage modulus of PVA, PVA/MMT, and PVA/MMT/TiO$_2$ systems. The loss factor is influenced by the
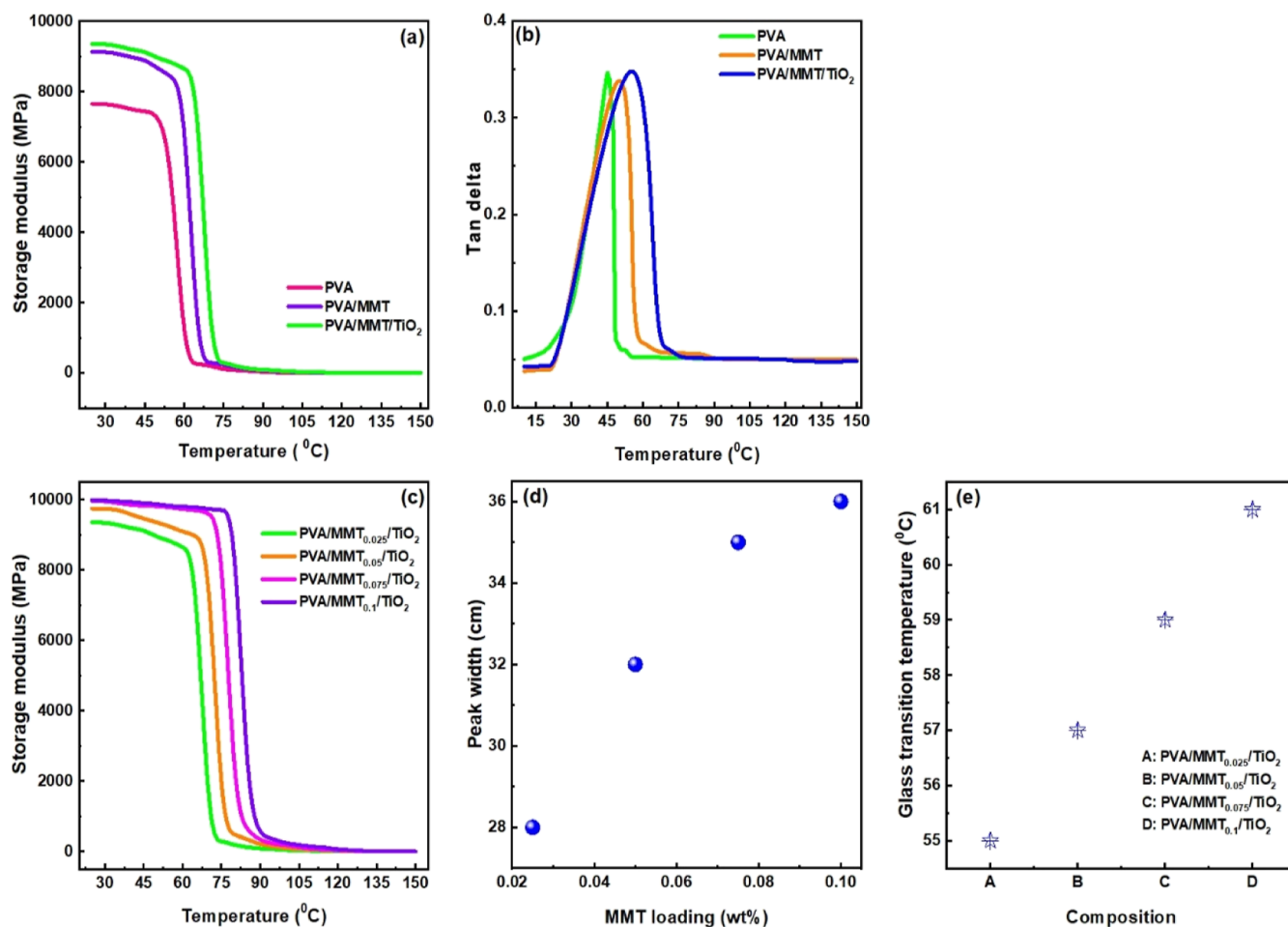
Figure 5. (a) Storage modulus vs temperature plot of PVA, PVA/MMT, and PVA/MMT/TiO$_2$ nanocomposite films. (b) tan δ vs temperature plot of PVA, PVA/MMT, and PVA/MMT/TiO$_2$ nanocomposite films. (c) Storage modulus with respect to MMT loading. (d) Peak width with respect to MMT loading. (e) Glass transition temperature with respect to composition.
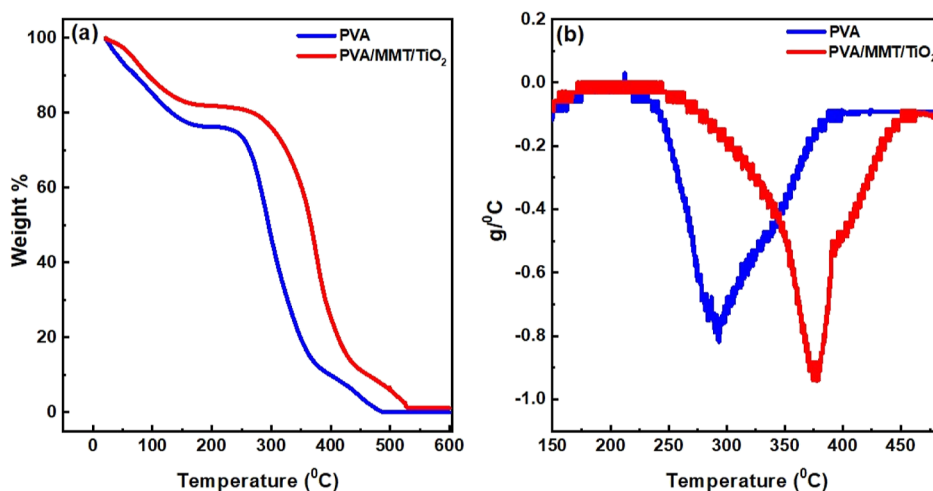

Figure 6. (a) TGA of PVA and PVA/MMT/TiO$_2$ nanocomposite films. (b) DTG of PVA and PVA/MMT/TiO$_2$ nanocomposite films.

incorporation of fillers in a composite system.[57] This may be attributed to the shear stress concentration at the filler ends in association with additional energy dissipation within the polymer matrix. It has been observed that the tan δ peak becomes more broadened in the case of the PVA/MMT/TiO$_2$ system than those of PVA and PVA/MMT systems. This is a clear indication of the embedding effect of MMT and TiO$_2$

nanoparticles within the PVA matrix. The systems function in a synchronized way under the dynamic load.

The tan δ peak width is an indication of increased free volume of the interface.[58] The peak width at half height of the samples from the damping curve is shown in Figure 5d. As the MMT loading increases, the peak width has been found to be increased. Increase in concentration of the filler increases the interfaces.[59]
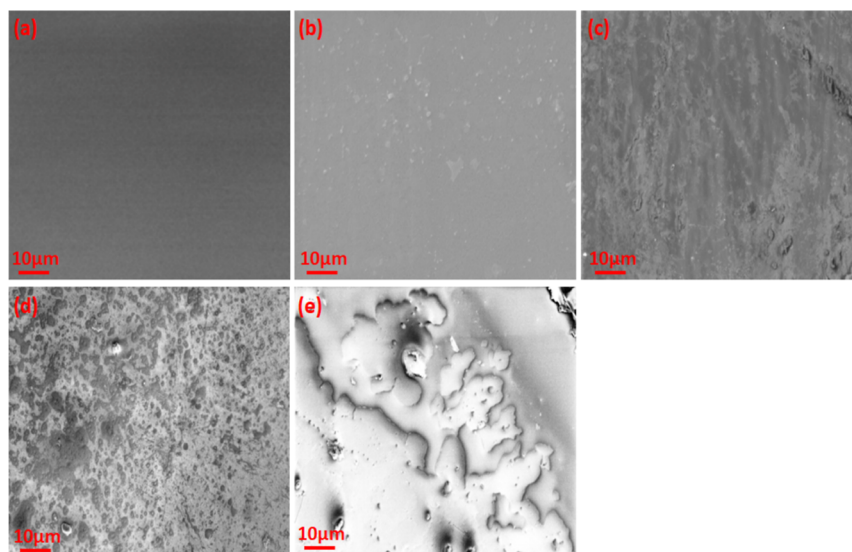
Figure 7. SEM images of (a) PVA, (b) PVA/TiO$_2$, (c) PVA/MMT, (d) PVA/MMT/TiO$_2$ (TiO$_2$ loading = 0.3 wt %), and (e) PVA/MMT/TiO$_2$ (TiO$_2$ loading = 0.5 wt %).
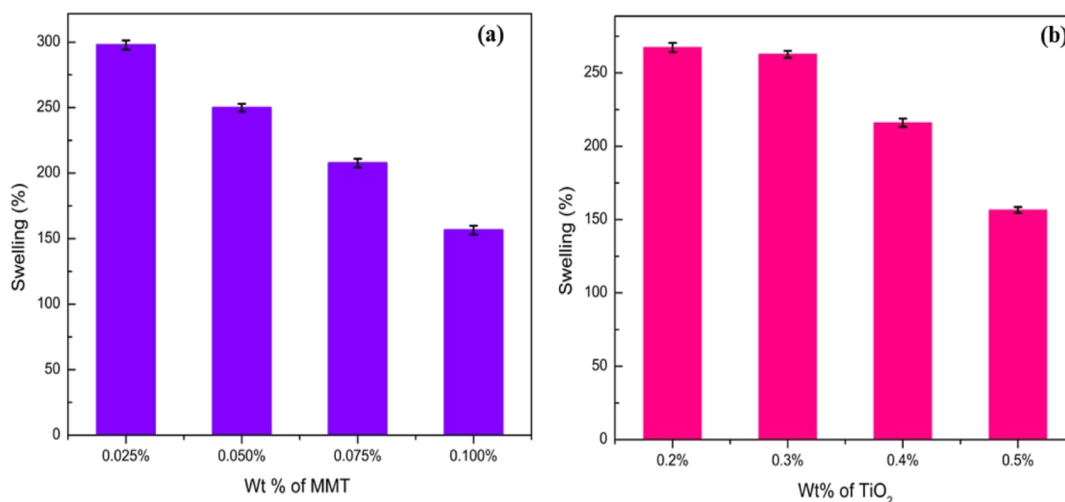

Figure 8. Variation of swelling (%) with respect to (a) MMT loading and (b) TiO$_2$ loading.

Stress induced motion may also occur in the composite system, which leads to the dissipation of energy and mechanical damping. Variation of glass transition temperature (T_g) with composition has been depicted as Figure 5e. Virgin PVA has a T_g of 46 °C, whereas the nanocomposite with 0.025 wt % MMT loading has a T_g of 55 °C. When the MMT loading increases to 0.1 wt %, the T_g become 61 °C. The shift in T_g may be attributed to the increased crystallinity of the nanocomposite and reduced segmental mobility, owing to the adhesion between the polymer matrix and the nanofillers.

Thermogravimetric Analysis. Thermograms of PVA and a representative PVA/MMT/TiO$_2$ nanocomposite film have been shown as Figure 6a. The major decomposition of PVA occurs at 293 °C, owing to the loss of volatile unsaturated aldehydes and other unsaturated compounds.[60] Introduction of MMT and TiO$_2$ into PVA increases the thermal stability of PVA and the major decomposition temperature has been shifted to 376 °C. A corresponding derivative TG plot has been shown as Figure 6b.

Surface Morphology. Figure 7 shows the SEM images of virgin PVA, PAV/TiO$_2$, PVA/MMT, and PVA/MMT/TiO$_2$ nanocomposite films. In the case of neat PVA, smooth and homogeneous surfaces have been observed, whereas the dispersed TiO$_2$ nanoparticles are visible in the SEM image of the PVA/TiO$_2$ nanocomposite film (Figure 7b, average particle size-20 nm). Incorporation of MMT in the PVA matrix creates some heterogeneity in the PVA matrix and the surface become more rougher than neat PVA. Some reports reveal that the clay loading at higher concentrations may lead to agglomeration, owing to the hydrophilicity and high surface energy.[61] Figure 7d,e shows the SEM images of the nanocomposite films at different loadings of TiO$_2$ nanoparticles, viz, 0.3 and 0.5 wt %, respectively.

A relatively uniform distribution of TiO$_2$ nanoparticles is seen in Figure 7d. However, in the case of 0.5 wt % TiO$_2$-loaded samples, particle agglomerations have been visible (Figure 7e). This has been attributed to the higher surface energy of TiO$_2$ nanoparticles at higher concentrations.[62]

Swelling Studies. The swelling ratio is an indication of the dimensional stability of the system. Virgin PVA showed a large dimensional change (high swelling ratio), whereas PVA reinforced with MMT and TiO$_2$ exhibited a small dimensional change (low swelling ratio) when exposed to a solvent. In other
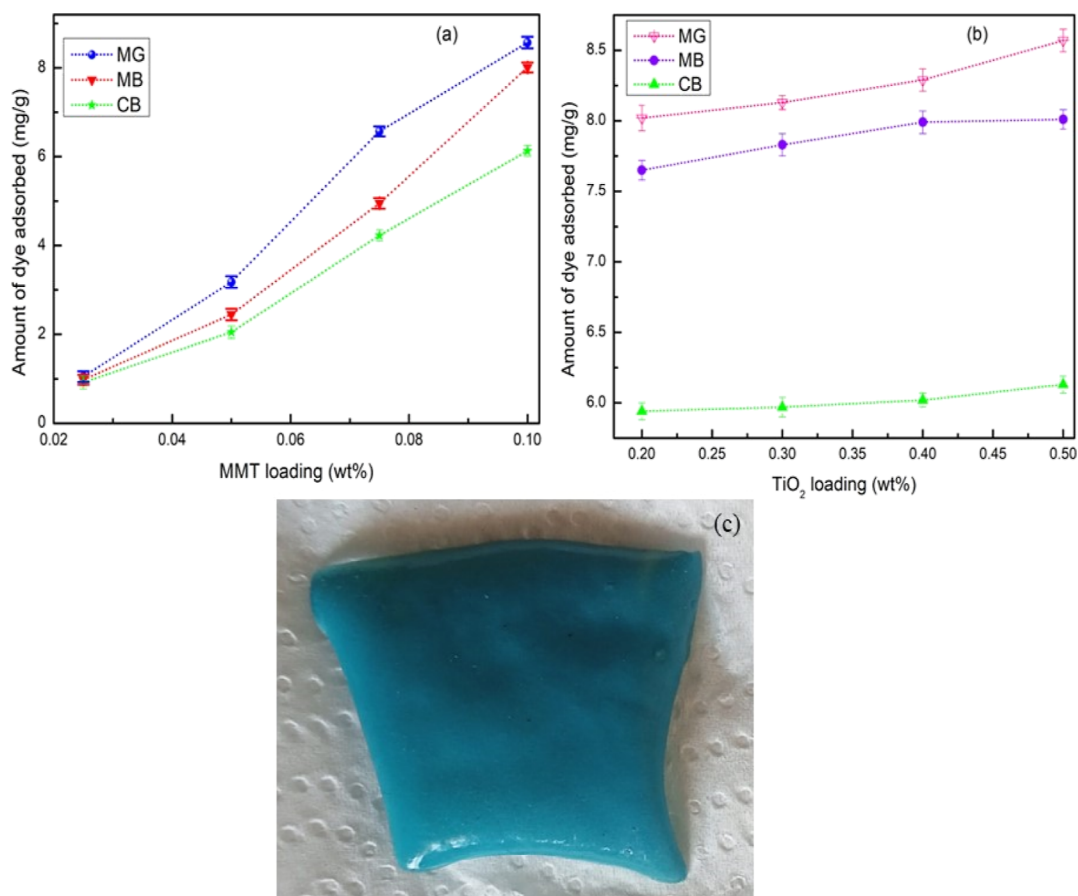
Figure 9. Amount of dye adsorbed at equilibrium (in mg/g) with respect to (a) MMT loading and (b) TiO_2 loading. (c) Photograph of a representative $PVA/MMT/TiO_2$ nanocomposite film after the adsorption of MG.

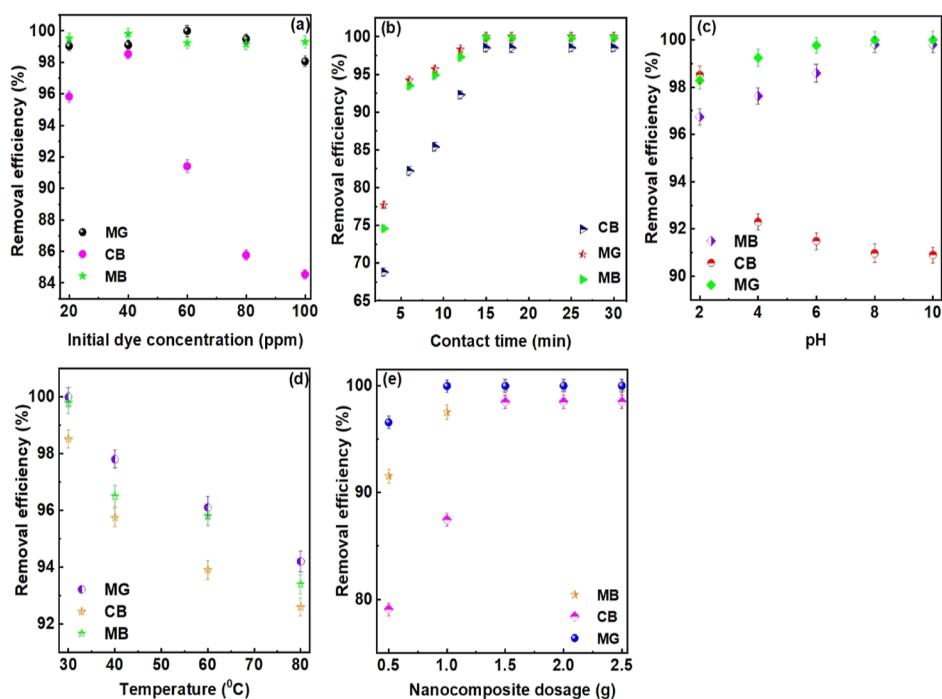**Figure 10.** Dye removal efficiency with respect to (a) initial dye concentration, (b) contact time, (c) pH, (d) temperature, and (e) nanocomposite dosage.

words, PVA yields to solvent stress readily, while the presence of MMT and TiO_2 offers further dimensional stability. For a

particular composition of the $PVA/MMT/TiO_2$ system, as the MMT loading increases, the swelling (%) has been observed to
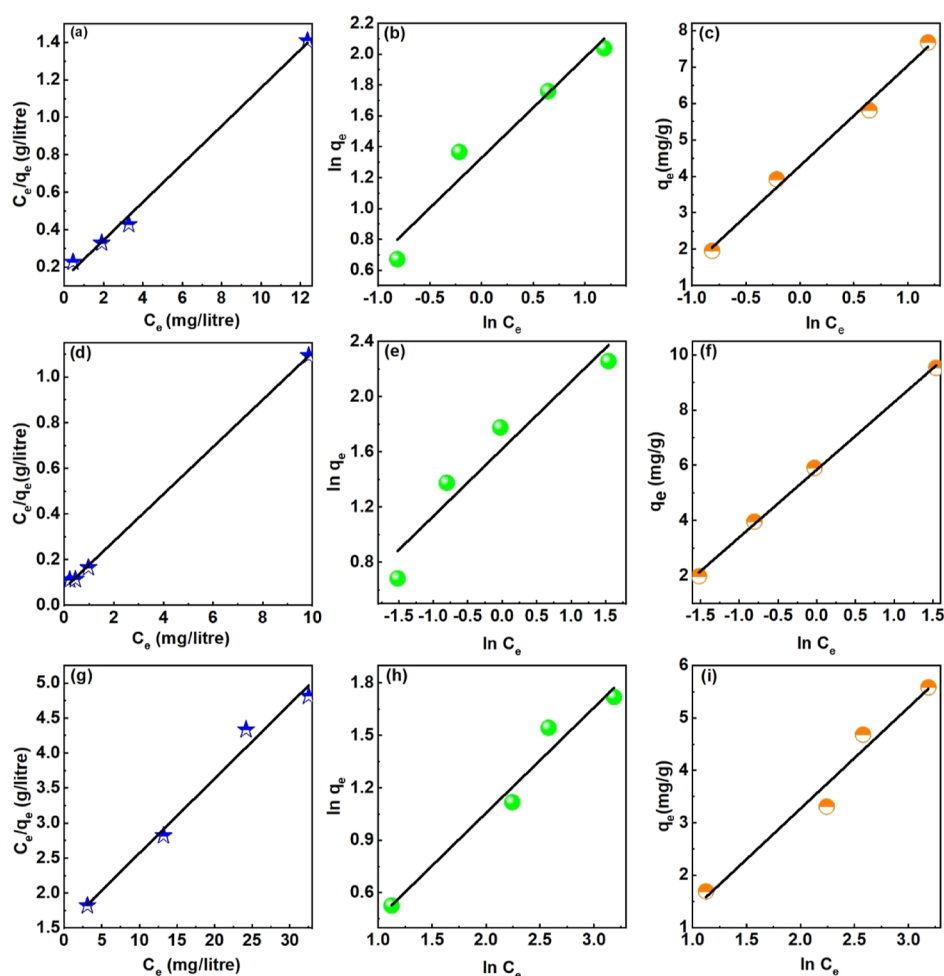
Figure 11. (a) Langmuir adsorption isotherm model for MB removal. (b) Freundlich adsorption isotherm model for MB removal. (c) Temkin adsorption isotherm model for MB removal. (d) Langmuir adsorption isotherm model for MG removal. (e) Freundlich adsorption isotherm model for MG removal. (f) Temkin adsorption isotherm model for MG removal. (g) Langmuir adsorption isotherm model for CB removal. (h) Freundlich adsorption isotherm model for CB removal. (i) Temkin adsorption isotherm model for CB removal.

Table 3. Adsorption Isotherm Data

dye	Langmuir model		Freundlich model			Temkin model		
	R_L	R_1^2	N	R_2^2	K_F	A_T	B	R_3^2
MG	0.011	0.998	1.54	0.9266	0.86	4.29	2.75	0.989
CB	0.125	0.975	1.66	0.9431	5.05	−0.59	1.93	0.950
MB	0.007	0.999	2.05	0.8837	3.77	5.84	2.45	0.998

be decreasing [Figure 8a]. Similar trends have been observed with TiO$_2$ loading as well [Figure 8b]. This is a clear indication of the effective reinforcement of PVA chains by embedded MMT and TiO$_2$ nanoparticles.

Dye Removal Studies. In the present work, a combination of adsorption and photocatalysis has been utilized for the dye removal. For the adsorption studies, PVA/MMT/TiO$_2$ nanocomposite films and the dye solutions, viz, MG, MB, and CB, respectively (60 ppm concentration), have been stirred under dark conditions. The solutions were then collected at regular time intervals, and the concentration of dye solutions has been examined by means of a UV−visible spectrophotometer. Figure 9a,b shows the variation of amount of dye adsorbed (in mg/g) with respect to MMT and TiO$_2$ loading, respectively (equilibrium time is 15 min).

It has been observed that the amount of dye adsorbed at equilibrium (milligrams per gram) increases as the MMT loading in the nanocomposite film increases. The TiO$_2$ dosage follows the same pattern as well; however, significant variations occurs with MMT loading. An increase in the loading of MMT and nano TiO$_2$ offers sufficient surface area and open adsorption sites. Therefore, the amount of dye adsorption increases with an increase in MMT and nano TiO$_2$.

As the MMT loading increases from 0.025 to 0.1 wt %, the amount of dye adsorption increases from 1.05 to 8.57 mg/g and from 0.98 to 8.01 mg/g for MG and MB, respectively. In the case of CB, the amount of dye adsorption increased from 0.92 to 6.13 mg/g. As the TiO$_2$ loading increases from 0.2 to 0.5 wt %, the MG and MB dye adsorption increases from 8.02 to 8.52 and 7.65 to 8.01 mg/g, respectively. Figure 9c shows the photograph of a
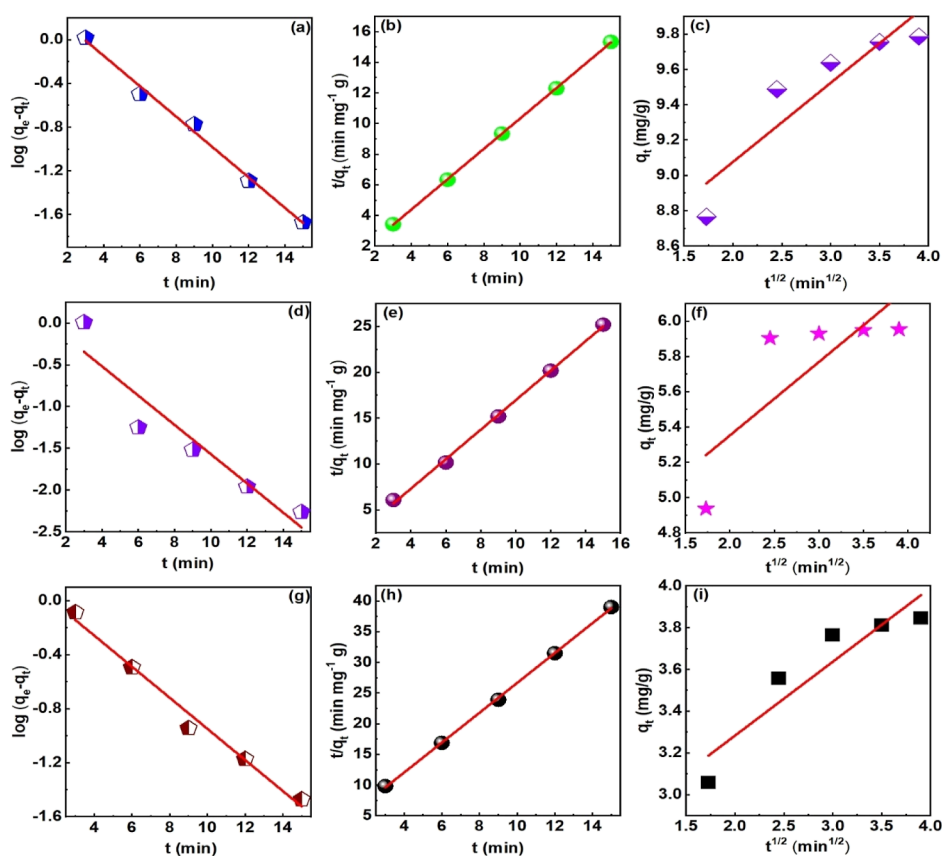
Figure 12. (a) Pseudo-first-order model for MB removal. (b) Pseudo-second-order model for MB removal. (c) Intraparticle diffusion models for MB removal. (d) Pseudo-first-order model for MG removal. (e) Pseudo-second-order model for MG removal. (f) Intraparticle diffusion models for MG removal. (g) Pseudo-first-order model for CB removal. (h) Pseudo-second-order model for CB removal. (i) Intraparticle diffusion models for CB removal.

Table 4. Kinetic Parameters for Dye Adsorption

	experimental	PFO model			PSO model			IPD model		
	q_e (mg g^{-1})	K_1 (min^{-1})	R^2	q_e (mg g^{-1})	K_2 (g mg min^{-1})	R^2	q_e (mg g^{-1})	K_{id} (g mg^{-1} min$^{1/2}$)	R^2	q_e (mg g^{-1})
MB	8.78	−0.03	0.9916	2.56	0.024	0.9999	9.10	0.1445	0.7906	8.158
CB	6.54	−0.025	0.9798	1.59	0.026	0.9996	4.11	0.114	0.8231	2.559
MG	9.02	−0.041	0.8616	1.51	0.026	0.9991	8.21	0.134	0.5281	4.498

Table 5. Thermodynamic Parameters for the Dye Adsorption

dyes	ΔG (kJ/mol)				ΔH (kJ/mol)	ΔS (J/mol)
	303 K	313 K	333 K	353 K		
MB	−12.26	−11.48	−9.93	−8.38	−35.75	−77.53
CB	−10.65	−9.89	−8.35	−6.82	−33.86	−76.59
MG	−13.63	−12.85	−11.30	−9.69	−37.33	−78.21

representative PVA/MMT/TiO$_2$ nanocomposite film after the adsorption of MG.

Optimization of Parameters: Adsorptive and Photocatalytic Dye Removal. For the adsorptive and photocatalytic dye removal studies, the PVA/MMT/TiO$_2$ nanocomposite film and the dye solutions, viz, MG, MB, and CB, respectively, have been stirred under direct sunlight. The solutions were then collected at regular time intervals and the concentration of dye solutions has been examined by means of a UV−visible spectrophotometer. Various parameters affecting the dye removal efficiency, such as effect of initial dye concentration,

contact time, pH, temperature, and the nanocomposite dosage, have been investigated in detail.

Effect of Initial Dye Concentration. The dye removal efficiency has been investigated with dye solutions having concentrations of 20, 40, 60, 80, and 100 ppm. A fixed amount of nanocomposite film (1 g) was added to every 100 mL of the dye solution. Figure 10a shows the variation of dye removal efficiency with respect to the initial concentration of dye solution. It has been observed that for MG, the highest removal efficiency of 99.99% was reached at a dye concentration of 60 ppm, while in the case of MB and CB, the 40 ppm solution gives highest removal efficiency, 99.79 and 98.52%, respectively. Greater concentration gradient between the dye molecules and the nanocomposite surface, significant number of empty adsorption sites on the nanocomposite film, as well as the formation of photoinduced active species on the nanocomposite surface may contribute to the enhanced dye removal efficiency. As the initial concentration of the dye solution increases more and more, the majority of the active sites have been occupied by dye molecules, and the nanocomposite surface attained a saturation point. Further, the adsorbed dye molecules inhibit the
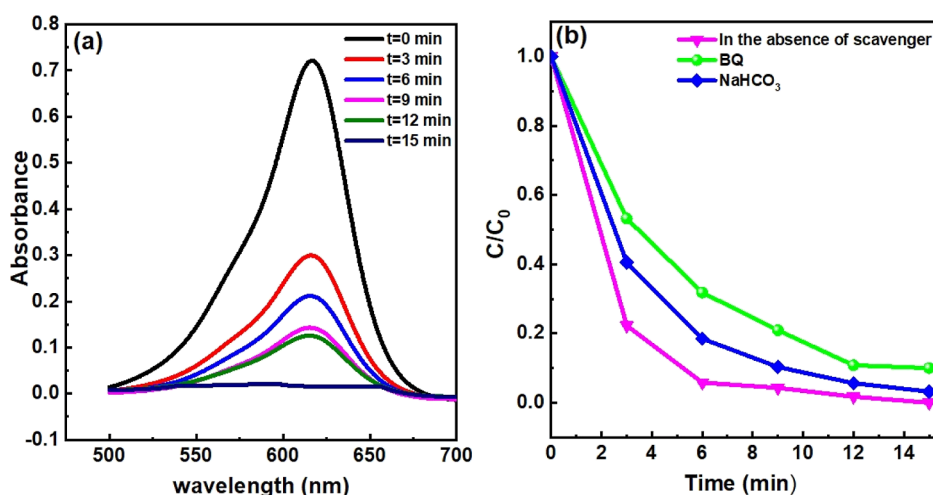
Figure 13. (a) UV−visible absorption spectra for the removal of a representative dye, viz, MG, with time. (b) Kinetics of photodegradation in the presence and absence of a scavenger.

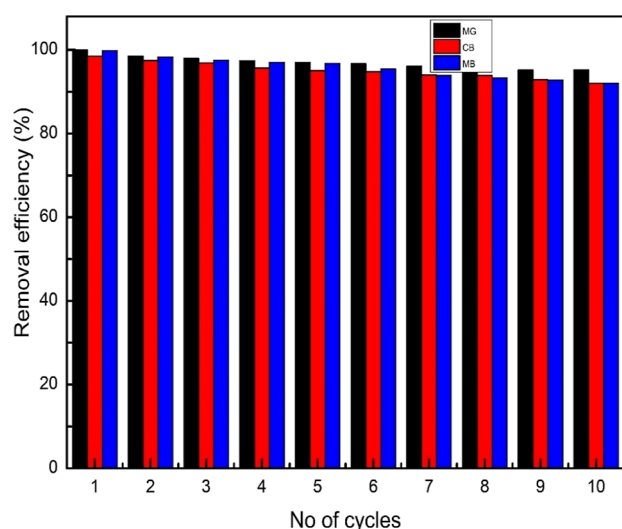**Figure 14.** Photographs showing photodegradation of the MG solution with respect to time.

Figure 15. Reusability studies on PVA/MMT/TiO$_2$ systems.

reaction of adsorbed molecules with photoinduced species. Similar observations have been reported by Daneshvar et al., 2003[63] and Grzechulska and Morawski 2002.[64]

Effect of Contact Time. To study the influence of contact time on the dye removal, the dye removal studies have been carried out at regular time intervals such as 3, 6, 9, 12, 15, 18, 25, and 30 min. Figure 10b shows the variation of dye removal efficiency with respect to contact time. It has been found that for all three dyes, the removal efficiency increases with increase in time and the maximum removal efficiency has been attained by 15 min. The presence of a significant number of active sites may have contributed to the initial increase in the removal efficiency. The limiting value has been achieved at 15 min and further increase in contact time does not influence the dye removal efficiency.

Effect of pH. It has been observed that the pH of the dye solution has a significant impact on its removal by the PVA/ MMT/TiO$_2$ system. The pH ranges selected for the studies were 2, 4, 6, 8, and 10. Figure 10c shows the variation of removal efficiency (%) with respect to pH. Removal efficiency of the cationic dyes MG and MB increases as the pH increases from 2 to 8. However, for the anionic CB dye, the maximum removal efficiency was attained at pH 2. The ionic interactions between the dye molecules and protonated hydroxyl groups of the nanocomposite film are responsible for their removal. The hydroxyl groups in the nanocomposite film become more protonated at an acidic pH, giving the surface a positive charge. MG and MB molecules ionize to form cationic dye ions in an aqueous solution. Reduced pH levels result in lower removal efficiency due to the mutual repulsion between these two positively charged species. The anionic dye CB, on the other

Table 6. Performance Evaluation of the Polymer Nanocomposite Employed for Dye Removal Studies

polymer nanocomposite	target dye	result	refs
nanocomposite film of present invention (PVA/MMT/TiO$_2$)	MG	highest removal efficiency of 99.99% at 60 ppm concentration, at pH 8 with 15 min exposure time	this work
	CB	removal efficiency of 98.52% at an optimal pH of 2 (exposure time: 15 min)	this work
	MB	highest removal efficiency of 99.79% at 60 ppm concentration, at pH 8 with 15 min exposure time	This work
chitosan/CuO nanocomposite beads	Congo red (CR) Eriochrome black T (EBT)	97% of dyes were removed within 2 h. Maximum adsorption capacity of CR and EBT were 119.70 and 235.70 mg g^{-1}	72
polypyrrole/zeolite nanocomposite	reactive blue (RB) reactive red (RR)	86.2% of RB and 88.3% of RR were adsorbed from synthetic solution	73
polylactic acid/graphene oxide/chitosan nanocomposite	crystal violet (CV)	97.8 ± 0.5% of CV was removed by 46 min	74
molecularly imprinted chitosan/TiO$_2$ nanocomposite	Rose Bengal (RB)	the adsorption capacity for RB was 79.365 mg/g (87%) and enthalpy was 62.279 kJ mol^{-1}. The optimized contact time is 20 min	75
poly(methyl methacrylate)/multiwall carbon nanotube nanocomposite	methyl green	the Langmuir adsorption capacity for methyl green was 6.85 mmol/g at 25 °C. The optimized contact time is 120 min	76
polyhydroxy butyrate/TiO$_2$	MB	96% of the MB solution was decolorized after 1 h solar illumination	77
chitosan/CdS	CR	85.9% of degradation rate was achieved within 180 min	78
poly(3-hexylthiophene)/TiO$_2$	methyl orange (MO)	the degradation rate of MO reached the maximum of 88.5% in 10 h under visible light	79
CuO−SiO$_2$/PVA	Nile blue (NB) MB	83% of NB degradation by 300 min and 76% MB degradation by 360 min	80
chitosan/ZnO nanocomposite	MB	96.7% of MB removal by 60 min	81
PVA/carbon dot@ZnO$_2$	MB	removal efficiency was 98% and optimized time is 60 min	82
polyacrylonitrile/graphene oxide−ZnO	Indigo carmine (IC) MB	98% of IC was removed by 27 min and 96% MB was removed by 70 min	83
pyrrole−thiophene/ZnO	MB	95.3% MB removal by 420 min	84
polyamidoamine/CuFe−O$_4$	Alizarin red (AR)	97% AR removal by 30 min	85
Fe$_3$O$_4$/activated carbon/cyclodextrin/alginate nanocomposites	MB	99.5% MB removal by 90 min (2.079 mg/g for polymer gel beads and 10.63 mg g^{-1} for dry powder beads)	86
magnetic polypyrrole/sodium alginate/CuFe$_2$O$_4$	direct blue 199	maximum adsorption capacity for direct blue 199 removal was 80.36 mg g^{-1} by 159 min	87
carboxymethyl cellulose-based 4-amino-phenazone@MWCNT nanocomposite	CV	maximum adsorption capacity was 22.4 mg/g by 50 min	88
chitosan/PVA/amino-functionalized montmorillonite nanocomposite electrospun membranes	basic blue	80% of the dye is removed after 15 min	89

hand, is more likely to bind to positively charged nanocomposite surfaces when the pH is acidic.

Effect of Temperature. The dye removal studies have been performed at different temperatures, viz, 30, 40, 60, and 80 °C. The effect of temperature on the removal of each dye was assessed and the results have been shown as Figure 10d. It has been observed that the dye removal efficiency decreases with an increase in temperature. This may be due to the reason that at elevated temperatures, the electrostatic interaction between the dye molecules and the nanocomposite films get weakened.[65,66]

Effect of Nanocomposite Dosage. To assess the impact of nanocomposite dosage on the dye removal, varying amounts of (0.5 1, 1.5, 2, and 2.5 g) PVA/MMT/TiO$_2$ nanocomposite films were added to 100 mL each of MG (60 ppm, pH 8), MB (40 ppm, pH 8), and CB (40 ppm, pH = 2). Variation of dye removal efficiency with respect to nanocomposite dosage is depicted in Figure 10e. It has been observed that as the weight of the nanocomposite increases from 0.5 to 1.5 g, the removal efficiency (%) for MG and MB increases from 96.57% to 99.99% and 91.55% to 99.78%, respectively, while in the case of CB, the removal efficiency increases from 79.06% to 98.51%. Therefore, the highest removal efficiency has been observed at 1.5 g of nanocomposite loading.

An increase in nanocomposite loading leads to an increase in the surface area, and the presence of additional active sites on the nanocomposite surface is the cause of this enhanced removal efficiency. As the amount of the PVA/MMT/TiO$_2$ nano-

composite film increases beyond 1.5 g, the dye removal efficiency has been observed to decline, owing to the decrease in the number of active sites, which arises due to the coagulation of the active species.

Adsorption Isotherm. To gain a comprehensive understanding of the dye adsorption mechanism, the adsorbate– adsorbent interactions, and the favorability of the adsorption process, we have investigated three adsorption isotherm models, viz, Langmuir, Freundlich, and Temkin models.[47,67]

According to Langmuir adsorption theory, adsorption takes place at certain homogeneous sites, generating a monolayer of noninteracting adsorbate molecules with equal adsorption heat. The linearized form of the Langmuir isotherm can be expressed by eq S1, (Supporting Information file). The Langmuir adsorption equilibrium constant K_L (L/g) is related to the rate of adsorption R_L as represented by eq S2. For favorable adsorption, the R_L values should be between 0 and 1. The plot of C_e/q_e versus C_e gives a straight graph having slope $(1/q_{max})$ and intercept $(1/K_L q_{max})$.

The heterogeneous multilayer adsorption with interacting adsorbent species is described by the Freundlich isotherm model and mathematically expressed as eq S3. Adsorption is favorable if the value of n is between 1 and 10, but a value lower than 1 is regarded as unfavorable. The adsorbate–adsorbent system's favorability and capacity are shown by the expression $1/n$.

The fundamental tenet of the Temkin isotherm model is that all molecular adsorption heat decreases linearly with increasing

adsorbent surface coverage. Up to a maximum binding energy, the adsorption exhibits a homogeneous distribution of binding energies. eq S4 can be used to describe the Temkin isotherm model.

In order to better understand the dye adsorption mechanism, the equilibrium adsorption data have been fitted with the isotherm models, and resulting plots have been shown as Figure 11. Table 3 shows the values of the correlation coefficients (R^2) and isotherm constants. The adsorption process has been found to be best fitted by the Langmuir model since the correlation coefficients are more closer to 1. It has been observed that the R_L values for all the three dyes are in the range of 0 and 1, suggesting the favorability of adsorption process.

Adsorption Kinetics. The kinetic models can be used to decipher the dye adsorption mechanism and potential rate controlling phases. In the current study, three kinetic models, viz; pseudo-first-order, pseudo-second-order, and intraparticle diffusion models, were used to analyze the kinetics and mechanism of the adsorption.[47,68]

The linear form of the pseudo-first-order kinetic model can be represented as eq S5. The plot of $\log(q_e - q_t)$ against "t" at various concentrations gives a linear curve with slope k_1 and intercept q_e.

The expression for the pseudo-second-order kinetic model is given as eq S6. The plot of t/q_t against t gives a straight line graph with q_e as the slope and k_2 as the intercept.

The intraparticle diffusion model can be mathematically expressed as eq S7. A linear or multilinear curve is expected from the plot of q_t versus $t^{1/2}$, which establishes the involvement of intraparticle diffusion in the adsorption process.

The experimental values of the dye adsorption process have been compared with pseudo-first-order, pseudo-second-order, and intraparticle diffusion models (Figure 12). The computed kinetic parameters, viz, K_1 (first-order rate constant), K_2 (second-order rate constant), and K_{id} (intraparticle diffusion rate constant), have been listed in Table 4. It has been shown that the experimental values have been found to be closer to pseudo-second-order models since the correlation coefficient is closer to 1.

Adsorption Thermodynamics. The thermodynamic equilibrium coefficients obtained at various temperatures were assessed to determine the adsorption thermodynamics. The mathematical relations used to estimate the thermochemical parameters that explain the feasibility, spontaneity, and the type of adsorbate−adsorbent interactions have been given as eqs S8−S10.[69,70]

From the slope and intercept of the linear plot $\ln K(q_e/c_e)$ vs $1/T$, the enthalpy change (ΔH) and entropy change (ΔS) can be determined. The standard Gibbs free energy (ΔG) has been evaluated by using the expression S9. The thermodynamic parameters for the dye adsorption are shown in Table 5. It can be seen that the ΔG is negative at all temperature ranges. The negative value of free energy indicates that the adsorption of dyes onto the nanocomposite film is spontaneous and feasible. The enthalpy of the process has been found to be negative, thus suggesting the exothermic nature of the adsorption. The negative value of ΔS indicates a reduction in the randomness during adsorption.

Figure 13a shows the UV−visible absorption spectra for the removal of a representative dye, viz, MG, with time. As the time increases, the intensity of absorption peak decreases and become almost a straight line by 15 min. Superoxide radicals ($O_2^{\bullet-}$) and photogenerated holes (h^+) are the possible reactive species involved in the photodegradation of dye molecules.[71] To understand the reactive species involved in the photo-degradation of a representative dye, MG, photocatalytic studies have been carried out by using different scavengers such as benzoquinone (BQ, $O_2^{\bullet-}$ scavenger, concentration = 10^{-3} mol/L) and NaHCO$_3$ (H$^+$ scavenger, concentration = 2×10^{-3} mol/L). They were separately introduced into the photodegradation system, and the photodegradation kinetics have been depicted as Figure 13b. As seen from Figure 13b, the absence of either $O_2^{\bullet-}$ or h$^+$ reduces the activity of photodegradation, revealing that both superoxide radicals and holes are simultaneously involved in MG degradation. Further, MG degradation has been observed to be decreased more by BQ, indicating that $O_2^{\bullet-}$ is the major active species in the degradation process.

Figure 14 shows the changes in color of a representative dye solution, MG, after treating with the nanocomposite film, with respect to time.

Reusability. Reusability of the nanocomposite film is an important factor as far as its practical application is concerned. The PVA/MMT/TiO$_2$ nanocomposite film has been subjected to consecutive reusability studies to validate the efficiency of the system. The desorption studies showed that PVA/MMT/TiO$_2$ nanocomposite films of the present invention exhibited excellent reusability. The same film can be used 10 times, without a significant reduction in the activity as shown in Figure 15.

Table 6 shows a comparison of the performance evaluation of some polymer nanocomposites employed for dye removal studies. From Table 6, it has been shown that the nano-composite film of the present invention exhibited excellent removal efficiency compared to those reported in the literature.

■ CONCLUSIONS

In the present work, PVA/MMT/TiO$_2$ nanocomposite films have been developed via a simple film casting strategy for the efficient removal of both cationic and anionic dyes. The nanocomposite photocatalyst film of the present invention has excellent chemical and thermal stability, mechanical properties, and dynamic mechanical characteristics. The mechanism of dye removal follows both adsorption and photocatalysis. The adsorption is best fitted by the Langmuir model and kinetics of adsorption follows the pseudo-second-order kinetic model. The spontaneity and hence the feasibility of the adsorption process has been confirmed from the negative value of free energy change. The dye removal studies in the presence of scavenger revealed that $O_2^{\bullet-}$ is the major active species involved in the degradation. The major achievements of the work are (1) the reusability of the nanocomposite film; the same film can be used for 10 cycles without a significant reduction in the activity and (2) the ease in the removal of the nanocomposite film from solution after treatment.

■ ASSOCIATED CONTENT

Data Availability Statement

The data underlying this study are available in the published article and its Supporting Information.

Ⓢ Supporting Information

The Supporting Information is available free of charge at https://pubs.acs.org/doi/10.1021/acsomega.4c06530.

> Adsorption isotherm, kinetics and thermodynamic parameters: calculation formulas (PDF)

AUTHOR INFORMATION

Corresponding Authors

Bindu Mavila − *Department of Environmental Studies, Kannur University, Kannur, Kerala 670567, India*; Email: binduscs@gmail.com

Pradeepan Periyat − *Department of Environmental Studies, Kannur University, Kannur, Kerala 670567, India;* orcid.org/0000-0001-8546-0994; Email: pperiyat@kannuruniv.ac.in

Authors

Hareesh Pradeep − *Department of Environmental Studies, Kannur University, Kannur, Kerala 670567, India*

Shwetha Suresh − *Department of Environmental Studies, Kannur University, Kannur, Kerala 670567, India*

Najiya Cheroor Konathodi − *Department of Environmental Studies, Kannur University, Kannur, Kerala 670567, India*

Anil Adukkadan − *Department of Materials Engineering, Indian Institute of Science, Bangalore, Karnataka 560012, India*

Monika Monika − *Department of Materials Engineering, Indian Institute of Science, Bangalore, Karnataka 560012, India*

Complete contact information is available at:
https://pubs.acs.org/10.1021/acsomega.4c06530

Author Contributions

§Bindu Mavila, Hareesh Pradeep, and Shwetha Suresh made equal contributions. Bindu Mavila: Conceptualization, Validation, Methodology, Investigation, Formal analysis, Data curation, Supervision, Writing-original draft, Writing-review and editing. Hareesh Pradeep: Investigation, Methodology, Formal analysis, Data curation, Writing—original draft. Shwetha Suresh: Investigation, Data curation. Najiya Cheroor Konathodi: Investigation, Data curation. Anil Adukkadan: Data curation. Monika Monika: Data curation. Pradeepan Periyat: Project administration, Supervision, Writing-review and editing.

Notes

The authors declare no competing financial interest.

ACKNOWLEDGMENTS

REFERENCES

(1) Liu, L.; Gao, Z. Y.; Su, X. P.; Chen, X.; Jiang, L.; Yao, J. M. Adsorption Removal of Dyes from Single and Binary Solutions Using a Cellulose-based Bioadsorbent. *ACS Sustainable Chem. Eng.* **2015**, *3*, 432−442.

(2) Gastaldi, M.; Cardano, F.; Zanetti, M.; Viscardi, G.; Barolo, C.; Bordiga, S.; Magdassi, S.; Fin, A.; Roppolo, I. Functional Dyes in Polymeric 3D Printing: Applications and Perspectives. *ACS Mater. Lett.* **2021**, *3*, 1−17.

(3) Othman, Z.; Sinopoli, A.; Mackey, H. R.; Mahmoud, K. A. Efficient Photocatalytic Degradation of Organic Dyes by AgNPs/TiO$_2$/Ti$_3$C$_2$T$_x$ MXene Composites under UV and Solar Light. *ACS Omega* **2021**, *6*, 33325−33338.

(4) Malik, B.; Sandhu, K. K. Occurrence and impact of heavy metals on environment. *Mater. Today Proc.* **2023**.

(5) Rashid, T. U.; Kabir, S. M. F.; Biswas, M. C.; Bhuiyan, M. A. R. Sustainable Wastewater Treatment via Dye-Surfactant Interaction: A Critical Review. *Ind. Eng. Chem. Res.* **2020**, *59* (21), 9719−9745.

(6) Özkan, B. Ç.; Fırat, M.; Chormey, D. S.; Bakırdere, S. Accurate and sensitive determination of harmful aromatic amine products of azo dyes in wastewater and textile samples by GC-MS after multivariate optimization of binary solvent dispersive liquid-liquid microextraction. *Microchem. J.* **2019**, *145*, 84−89.

(7) Feng, Y.; Chen, S.; Zhao, Y.; Wu, D.; Li, G. Heterocyclic aromatic amines induce Neuro-2a cells cytotoxicity through oxidative stress-mediated mitochondria-dependent apoptotic signals. *Food Chem. Toxicol.* **2022**, *168*, 113376.

(8) Dutta, S.; Gupta, B.; Srivastava, S. K.; Gupta, A. K. Recent advances on the removal of dyes from wastewater using various adsorbents: a critical review. *Mater. Adv.* **2021**, *2*, 4497−4531.

(9) Tian, X.; Zhu, H.; Meng, X.; Wang, J.; Zheng, C.; Xia, Y.; Xiong, Z. Amphiphilic Calcium Alginate Carbon Aerogels: Broad-Spectrum Adsorbents for Ionic and Solvent Dyes with Multiple Functions for Decolorized Oil-Water Separation. *ACS Sustainable Chem. Eng.* **2020**, *8*, 12755−12767.

(10) Osman, A. I.; Elgarahy, A. M.; Mehta, N.; Al-Muhtaseb, A. H.; Al-Fatesh, A. S.; Rooney, D. W. Facile Synthesis and Life Cycle Assessment of Highly Active Magnetic Sorbent Composite Derived from Mixed Plastic and Biomass Waste for Water Remediation. *ACS Sustainable Chem. Eng.* **2022**, *10*, 12433−12447.

(11) Wang, Y.; Geng, Q.; Yang, J.; Liu, Y.; Liu, C. Hybrid System of Flocculation-Photocatalysis for the Decolorization of Crystal Violet, Reactive Red X-3B and Acid Orange II Dye. *ACS Omega* **2020**, *5*, 31137−31145.

(12) Anucha, C. B.; Altin, I.; Bacaksiz, E.; Stathopoulos, V. N. Titanium dioxide (TiO$_2$)-based photocatalyst materials activity enhancement for contaminants of emerging concern (CECs) degradation: In the light of modification strategies. *Chem. Eng. J. Adv.* **2022**, *10*, 100262.

(13) Rafique, M.; Hajra, S.; Irshad, M.; Usman, M.; Imran, M.; Assiri, M. A.; Ashraf, W. M. Hydrogen Production Using TiO$_2$-Based Photocatalysts: A Comprehensive Review. *ACS Omega* **2023**, *8*, 25640−25648.

(14) Li, X.; Chen, Y.; Tao, Y.; Shen, Li.; Xu, Z.; Bian, Z.; Li, H. Challenges of photocatalysis and their coping strategies. *Chem Catal.* **2022**, *2*, 1315−1345.

(15) Zhang, F.; Wang, X.; Liu, H.; Liu, C.; Wan, Y.; Long, Y.; Cai, Z. Recent Advances and Applications of Semiconductor Photocatalytic Technology. *Appl. Sci.* **2019**, *9*, 2489.

(16) Qutub, N.; Singh, P.; Sabir, S.; Sagadevan, S.; Oh, W. C. Enhanced photocatalytic degradation of Acid Blue dye using CdS/TiO$_2$ nanocomposite. *Sci. Rep.* **2022**, *12*, 5759.

(17) Homocianu, M.; Pascariu, P. High-performance photocatalytic membranes for water purification in relation to environmental and operational parameters. *J. Environ. Manage.* **2022**, *311*, 114817.

(18) Padmanabhan, N. T.; Thomas, N.; Louis, J.; Mathew, D. T.; Ganguly, P.; John, H.; Pillai, S. C. Graphene coupled TiO$_2$ photocatalysts for environmental applications: A review. *Chemosphere* **2021**, *271*, 129506.

(19) Xiong, P.; Xu, S.; Yang, T.; Jing, K. Novel Silanized Graphene Oxide/TiO$_2$ Multifunctional Nanocomposite Photocatalysts: Simultaneous Removal of Cd^{2+} and Photodegradation of Phenols under Visible Light Irradiation. *ACS Omega* **2021**, *6*, 28813−28827.

(20) Pourmorteza, N.; Jafarpour, M.; Feizpour, F.; Rezaeifard, A. TiO$_2$ nanoparticles decorated with Co-Schiff base-g-C$_3$N$_4$ as an efficient photocatalyst for one-pot visible light-assisted synthesis of benzimidazoles. *RSC Adv.* **2022**, *12*, 22526−22541.

(21) Asiltürk, M.; Sener, S. TiO$_2$-activated carbon photocatalysts: Preparation, characterization and photocatalytic activities. *Chem. Eng. J.* **2012**, *180*, 354−363.

(22) Djordjevic, A.; Šojić Merkulov, D.; Lazarevic, M.; Borišev, I.; Medić, I.; Pavlović, V.; Miljevic, B.; Abramović, B. Enhancement of nano titanium dioxide coatings by fullerene and polyhydroxy fullerene in the photocatalytic degradation of the herbicide mesotrione. *Chemosphere* **2018**, *196*, 145−152.

(23) Yang, H.; Zhang, J.; Song, Y.; Xu, S.; Jiang, L.; Dan, Y. Visible light photo-catalytic activity of C-PVA/TiO$_2$ composites for degrading rhodamine B. *Appl. Surf. Sci.* **2015**, *324*, 645−651.

(24) Markowska-Szczupak, A.; Rokicka, P.; Wang, K.; Endo, M.; Morawski, A. W.; Kowalska, E. Photocatalytic Water Disinfection under Solar Irradiation by d-Glucose-Modified Titania. *Catalysts* **2018**, *8*, 316.

(25) Chen, S. H.; Hsiao, Y. C.; Chiu, Y. J.; Tseng, Y. H. A Simple Route in Fabricating Carbon-Modified Titania Films with Glucose and Their Visible-Light-Responsive Photocatalytic Activity. *Catalysts* **2018**, *8*, 178.

(26) Hegedűs, P.; Szabó-Bárdos, E.; Horváth, O.; Szabó, P.; Horváth, K. Investigation of a TiO₂ photocatalyst immobilized with poly(vinyl alcohol). *Catal. Today* **2017**, *284*, 179−186.

(27) Dehghani, M. T.; Delnavaz, M. UV-light-responsive Ag/TiO₂/PVA nanocomposite for photocatalytic degradation of Cr, Ni, Zn, and Cu heavy metal ions. *Sci. Rep.* **2024**, *14*, 5195.

(28) Huang, J.; Yu, H.; Abdalkarim, S. Y. H.; Marek, J.; Militky, J.; Li, Y.; Yao, J. Electrospun polyethylene glycol/polyvinyl alcohol composite nanofibrous membranes as shape-stabilized solid-solid phase change materials. *Adv. Fiber Mater.* **2020**, *2*, 167−177.

(29) Dong, L.; Wang, M.; Wu, J.; Zhu, C.; Shi, J.; Morikawa, H. Deformable Textile-Structured Triboelectric Nanogenerator Knitted with Multifunctional Sensing Fibers for Biomechanical Energy Harvesting. *Adv. Fiber Mater.* **2022**, *4*, 1486−1499.

(30) Chen, Z.; Liu, H.; Lin, X.; Mei, X.; Lyu, W.; Liao, Y. Competitive proton-trapping strategy enhanced anti-freezing organo-hydrogel fibers for high-strain-sensitivity wearable sensors. *Mater. Horiz.* **2023**, *10*, 3569−3581.

(31) Xue, T.; Zhu, C.; Feng, X.; Wali, Q.; Fan, W.; Liu, T. Polyimide aerogel fibers with controllable porous microstructure for super-thermal insulation under extreme environments. *Adv. Fiber Mater.* **2022**, *4*, 1118−1128.

(32) Liu, H.; Chen, Z.; Lin, X.; Zhang, X.; Cai, Y.; Zhang, Y.; Sun, B.; Mei, X.; Lyu, W.; Kaner, R. B.; Zhu, M.; Liao, Y. A nanophase separation strategy toward organo-hydrogel fibrous sensors with ultralow detection limit and high strain sensitivity. *Chem. Mater.* **2024**, *36*, 6100−6113.

(33) Li, S.; Li, Y.; Wang, Y.; Pan, H.; Sun, J. Highly Stretchable, Elastic, Healable, and Ultra-Durable Polyvinyl Alcohol-Based Ionic Conductors Capable of Safe Disposal. *CCS Chem.* **2022**, *4*, 3170−3180.

(34) Ben Halima, N. Poly (vinyl alcohol): review of its promising applications and insights into biodegradation. *RSC Adv.* **2016**, *6*, 39823−39832.

(35) Lin, D.; Li, Y.; Huang, Y.; Qin, W.; Loy, D. A.; Chen, H.; Zhang, Q.; Wu, Z. Properties of polyvinyl alcohol films reinforced by citric acid modified cellulose nanocrystals and silica aerogels. *Carbohydr. Polym.* **2022**, *298*, 120116.

(36) Majeed, K.; Ahmed, A.; Abu Bakar, M. S.; Indra Mahlia, T. M.; Saba, N.; Hassan, A.; Jawaid, M.; Hussain, M.; Iqbal, J.; Ali, Z. Mechanical and Thermal Properties of Montmorillonite-Reinforced Polypropylene/Rice Husk Hybrid Nanocomposites. *Polymers* **2019**, *11*, 1557.

(37) Xu, J.; Cheng, L.; Zhang, Z.; Zhang, L.; Xiong, C.; Huang, W.; Xie, Y.; Yang, L. Highly exfoliated montmorillonite clay reinforced thermoplastic polyurethane elastomer: in situ preparation and efficient strengthening. *RSC Adv.* **2019**, *9*, 8184−8196.

(38) Lyu, W.; Li, J.; Trchov, M.; Wang, G.; Liao, Y.; Bober, P.; Stejskal, J. Fabrication of polyaniline/poly(vinyl alcohol)/montmorillonite hybrid aerogels toward efficient adsorption of organic dye pollutants. *J. Hazard. Mater.* **2022**, *435*, 129004.

(39) Qiu, J.; Cui, K.; Wu, P.; Chen, G.; Wang, Y.; Liu, D.; Jiang, S.; Wang, G. The adsorption characteristics and mechanism of montmorillonite with different layer charge density for alkyl ammonium with different carbon chain length. *New J. Chem.* **2021**, *45*, 10331−10339.

(40) Sharma, P.; Borah, D. J.; Das, P.; Das, M. R. Cationic and anionic dye removal from aqueous solution using montmorillonite clay: evaluation of adsorption parameters and mechanism. *Desalin. Water Treat.* **2016**, *57*, 8372−8388.

(41) Al Kausor, M.; Gupta, S. S.; Bhattacharyya, K. G.; Chakrabortty, D. Montmorillonite and modified montmorillonite as adsorbents for removal of water soluble organic dyes: A review on current status of the art. *Inorg. Chem. Commun.* **2022**, *143*, 109686.

(42) Zango, Z. U.; Garba, A.; Garba, Z. N.; Zango, M. U.; Usman, F.; Lim, J. W. Montmorillonite for Adsorption and Catalytic Elimination of Pollutants from Wastewater: A State-of-the-Arts Review. *Sustainability* **2022**, *14*, 16441.

(43) Parra, R.; Goes, M. S.; Castro, M. S.; Longo, E.; Bueno, P. R.; Varela, J. A. Reaction Pathway to the Synthesis of Anatase via the Chemical Modification of Titanium Isopropoxide with Acetic Acid. *Chem. Mater.* **2008**, *20*, 143−150.

(44) M, B.; Unnikrishnan, G. Transport features of nano-hydroxylapatite (n-HA) embedded silicone rubber (SR) systems: influence of SR/n-HA interaction, degree of reinforcement and morphology. *Phys. Chem. Chem. Phys.* **2017**, *19*, 25380−25390.

(45) Lv, Q.; Wu, M.; Shen, Y. Enhanced swelling ratio and water retention capacity for novel super-absorbent hydrogel. *Colloids Surf., A* **2019**, *583*, 123972.

(46) Cınar, S.; Kaynar, U. H.; Aydemir, T.; Çam Kaynar, S.; Ayvacikli, M. An efficient removal of RB5 from aqueous solution by adsorption onto nano-ZnO/Chitosan composite beads. *Int. J. Biol. Macromol.* **2017**, *96*, 459−465.

(47) Satheesh Kumar, K. V.; Bindu, M.; Suresh, S.; Anil, A.; Sujoy, S.; Mohanan, A.; Periyat, P. Investigation on swelling behavior of sodium alginate/black titania nanocomposite hydrogels and effect of synthesis conditions on water uptake. *Results Eng.* **2023**, *20*, 101460.

(48) Vahidhabanu, S.; Karuppasamy, D.; Adeogun, A. I.; Babu, B. R. Impregnation of zinc oxide modified clay over alginate beads: a novel material for the effective removal of Congo red from wastewater. *RSC Adv.* **2017**, *7*, 5669−5678.

(49) Dai, H.; Huang, Y.; Huang, H. Eco-friendly polyvinyl alcohol/carboxymethyl cellulose hydrogels reinforced with graphene oxide and bentonite for enhanced adsorption of methylene blue. *Carbohydr. Polym.* **2018**, *185*, 1−11.

(50) Chen, Y. N.; Jiao, C.; Zhao, Y.; Zhang, J.; Wang, H. Self-Assembled Polyvinyl Alcohol-Tannic Acid Hydrogels with Diverse Microstructures and Good Mechanical Properties. *ACS Omega* **2018**, *3*, 11788−11795.

(51) Park, J. H.; Karim, M. R.; Kim, I. K.; Cheong, I. W.; Kim, J. W.; Bae, D. G.; Cho, J. W.; Yeum, J. H. Electrospinning fabrication and characterization of poly(vinyl alcohol)/montmorillonite/silver hybrid nanofibers for antibacterial applications. *Colloid Polym. Sci.* **2010**, *288*, 115−121.

(52) Mansur, H. S.; Sadahira, C. M.; Souza, A. N.; Mansur, A. A. P. FTIR spectroscopy characterization of poly (vinyl alcohol) hydrogel with different hydrolysis degree and chemically crosslinked with glutaraldehyde. *Mater. Sci. Eng., C* **2008**, *28*, 539−548.

(53) Danková, Z.; Mockovčiaková, A.; Dolinská, S. Influence of ultrasound irradiation on cadmium cations adsorption by montmorillonite. *Desalin. Water Treat.* **2014**, *52*, 5462−5469.

(54) Gu, J.; Tian, W.; Wang, Z.; Ma, N.; Du, P. Control of Oxygen Vacancies in TiO₆ Octahedra of Amorphous BaTiO₃ Thin Films with Tunable Built-In Electric Field in a-BaTiO₃/p-Si Heterojunction for Metal-Oxide-Semiconductor Applications. *Phys. Status Solidi A* **2020**, *217*, 1900941.

(55) Oleyaei, S. A.; Almasi, H.; Ghanbarzadeh, B.; Moayedi, A. A. Synergistic reinforcing effect of TiO₂ and montmorillonite on potato starch nanocomposite films: Thermal, mechanical and barrier properties. *Carbohydr. Polym.* **2016**, *152*, 253−262.

(56) Achachlouei, B. F.; Zahedi, Y. Fabrication and characterization of CMC-based nanocomposites reinforced with sodium montmorillonite and TiO₂ nanomaterials. *Carbohydr. Polym.* **2018**, *199*, 415−425.

(57) Aradhya, R.; Rajan, J. S. Dynamic mechanical analysis for assessment of carbon fillers in glass fiber epoxy composites. *Polym. Compos.* **2023**, *44*, 6691−6706.

(58) Bindu, M.; Unnikrishnan, G. Modulation of dielectric and viscoelastic features of silicone rubber (SR) by nano-hydroxylapatite (n-HA) embedding. *New J. Chem.* **2018**, *42*, 6441−6448.

(59) Zhu, J.; Abeykoon, C.; Karim, N. Investigation into the effects of fillers in polymer processing. *Int. J. Lightweight Mater. Manuf.* **2021**, *4*, 370−382.

(60) Yang, H.; Xu, S.; Jiang, L.; Dan, Y. Thermal Decomposition Behavior of Poly (Vinyl Alcohol) with Different Hydroxyl Content. *J. Macromol. Sci., Part B: Phys.* **2012**, *51*, 464−480.

(61) Naidu, D. S.; John, M. J. Effect of Clay Nanofillers on the Mechanical and Water Vapor Permeability Properties of Xylan-Alginate Films. *Polymers* **2020**, *12*, 2279.

(62) Pellegrino, F.; Pellutiè, L.; Sordello, F.; Minero, C.; Ortel, E.; Hodoroaba, V. D.; Maurino, V. Influence of agglomeration and aggregation on the photocatalytic activity of TiO$_2$ nanoparticles. *Appl. Catal., B* **2017**, *216*, 80−87.

(63) Daneshvar, N.; Salari, D.; Khataee, A. R. Photocatalytic degradation of azo dye acid red 14 in water: investigation of the effect of operational parameters. *J. Photochem. Photobiol., A* **2003**, *157*, 111−116.

(64) Grzechulska, J.; Morawski, A. W. Photocatalytic decomposition of azo-dye acid black 1 in water over modified titanium dioxide. *Appl. Catal., B* **2002**, *36*, 45−51.

(65) Senthil Kumar, P.; Fernando, P. S. A.; Ahmed, R. T.; Srinath, R.; Priyadharshini, M.; Vignesh, A. M.; Thanjiappan, A. Effect of temperature on the adsorption of methylene blue dye onto sulfuric acid-treated orange Peel. *Chem. Eng. Commun.* **2014**, *201*, 1526−1547.

(66) Adeyemo, A. A.; Adeoye, I. O.; Bello, O. S. Adsorption of dyes using different types of clay: A review. *Appl. Water Sci.* **2017**, *7*, 543−568.

(67) El Jery, A.; Alawamleh, H. S.; Sami, M. H.; Abbas, H. A.; Sammen, S. S.; Ahsan, A.; Imteaz, M. A.; Shanableh, A.; Shafiquzzaman, M.; Osman, H.; Al-Ansari, N. Isotherms, kinetics and thermodynamic mechanism of methylene blue dye adsorption on synthesized activated carbon. *Sci. Rep.* **2024**, *14*, 970.

(68) Wawrzkiewicz, M.; Frynas, S.; Podkościelna, B. Synthesis and Characterization of Phosphorus-Containing Sorbent for Basic Dye Removal. *Molecules* **2023**, *28*, 6731.

(69) Sharma, K.; Vyas, R. K.; Dalai, A. K. Thermodynamic and Kinetic Studies of Methylene Blue Degradation Using Reactive Adsorption and its Comparison with Adsorption. *J. Chem. Eng. Data* **2017**, *62*, 3651−3662.

(70) Gharbani, P.; Mehrizad, A.; Mosavi, S. A. Optimization, kinetics and thermodynamics studies for photocatalytic degradation of Methylene Blue using cadmium selenide nanoparticles. *npj Clean Water* **2022**, *5*, 34.

(71) Pavel, M.; Anastasescu, C.; State, R. N.; Vasile, A.; Papa, F.; Balint, I. Photocatalytic Degradation of Organic and Inorganic Pollutants to Harmless End Products: Assessment of Practical Application Potential for Water and Air Cleaning. *Catalysts* **2023**, *13*, 380.

(72) Srivastava, V.; Choubey, A. K. Investigation of adsorption of organic dyes present in wastewater using chitosan beads immobilized with biofabricated CuO nanoparticles. *J. Mol. Struct.* **2021**, *1242*, 130749.

(73) Senguttuvan, S.; Janaki, V.; Senthilkumar, P.; Kamala-Kannan, S. Polypyrrole/zeolite composite-A nano adsorbent for reactive dyes removal from synthetic solution. *Chemosphere* **2022**, *287*, 132164.

(74) Zhou, G.; Wang, K. P.; Liu, H. W.; Wang, L.; Xiao, X. F.; Dou, D. D.; Fan, Y. B. Three-dimensional polylactic acid@graphene oxide/chitosan sponge bionic filter: Highly efficient adsorption of crystal violet dye. *Int. J. Biol. Macromol.* **2018**, *113*, 792−803.

(75) Ahmed, M. A.; Abdelbar, N. M.; Mohamed, A. A. Molecular imprinted chitosan-TiO$_2$ nanocomposite for the selective removal of Rose Bengal from wastewater. *Int. J. Biol. Macromol.* **2018**, *107*, 1046−1053.

(76) Hussein, M. A.; Albeladi, H. K.; Elsherbiny, A. S.; El-Shishtawy, R. M.; Al-romaizan, A. N. Cross-linked poly(methyl methacrylate)/multiwall carbon nanotube nanocomposites for environmental treatment. *Adv. Polym. Technol.* **2018**, *37*, 3240−3251.

(77) Yew, S.-P.; Tang, H. Y.; Sudesh, K. Photocatalytic activity and biodegradation of polyhydroxybutyrate films containing titanium dioxide. *Polym. Degrad. Stab.* **2006**, *91*, 1800−1807.

(78) Zhu, H.; Jiang, R.; Xiao, L.; Chang, Y.; Guan, Y.; Li, X.; Zeng, G. Photocatalytic decolorization and degradation of Congo Red on innovative crosslinked chitosan/nano-CdS composite catalyst under visible light irradiation. *J. Hazard. Mater.* **2009**, *169*, 933−940.

(79) Wang, D.; Zhang, J.; Luo, Q.; Li, X.; Duan, Y.; An, J. Characterization and photocatalytic activity of poly(3-hexylthiophene)-modified TiO$_2$ for degradation of methyl orange under visible light. *J. Hazard. Mater.* **2009**, *169*, 546−550.

(80) Yaseen, M.; Khan, A.; Humayun, M.; Bibi, S.; Farooq, S.; Bououdina, M.; Ahmad, S. Fabrication and characterization of CuO-SiO$_2$/PVA polymer nanocomposite for effective wastewater treatment and prospective biological applications. *Green Chem. Lett. Rev.* **2024**, *17*, 2321251.

(81) Mostafa, M. H.; Elsawy, M. A.; Darwish, M. S. A.; Hussein, L. I.; Abdaleem, A. H. Microwave-Assisted preparation of Chitosan/ZnO nanocomposite and its application in dye removal. *Mater. Chem. Phys.* **2020**, *248*, 122914.

(82) El-Shamy, A. G. An Efficient Removal of Methylene Blue Dye by Adsorption onto Carbon Dot @ Zinc Peroxide Embedded Poly Vinyl Alcohol (PVA/CZnO2) Nanocomposite: A Novel Reusable Adsorbent. *Polymer* **2020**, *202*, 122565.

(83) Abdel-Mottaleb, M. M.; Khalil, A.; Karim, S.; Osman, T.; Khattab, A. High Performance of PAN/GO-ZnO Composite Nanofibers for Photocatalytic Degradation Under Visible Irradiation. *J. Mech. Behav. Biomed. Mater.* **2019**, *96*, 118−124.

(84) Rahman, S.; Khan, M. M. R.; Deb, B.; Dana, S. I.; Ahmed, M. K. Effective and Simple fabrication of Pyrrole and Thiophene-Based Poly (Py-co-Th)/ZnO Composites for High photocatalytic Performance. *S. Afr. J. Chem. Eng.* **2023**, *43*, 303.

(85) Afshar, E. A.; Taher, M. A. New fabrication of CuFe$_2$O$_4$/PAMAM nanocomposites by an efficient removal performance for organic dyes: Kinetic study. *Environ. Res.* **2022**, *204*, 112048.

(86) Yadav, S.; Asthana, A.; Chakraborty, R.; Jain, B.; Singh, A. K.; Carabineiro, S. A. C.; Susan, M. A. B. H. Cationic Dye Removal Using Novel Magnetic/Activated Charcoal/β-Cyclodextrin/Alginate Polymer Nanocomposite. *Nanomaterials* **2020**, *10*, 170.

(87) Sadeghnezhad, M.; Ghorbani, M.; Nikzad, M. Synthesis of magnetic polypyrrole modified sodium alginate nanocomposite with excellent antibacterial properties and optimization of dye removal performance using RSM. *Ind. Crops Prod.* **2022**, *186*, 115192.

(88) Althomali, R. H.; Alamry, K. A.; Hussein, M. A.; Guedes, R. M. An investigation on the adsorption and removal performance of a carboxymethylcellulose-based 4-aminophenazone@MWCNT nanocomposite against crystal violet and brilliant green dyes. *RSC Adv.* **2023**, *13*, 4303−4313.

(89) Hosseini, S. A.; Daneshvar e Asl, S.; Vossoughi, M.; Simchi, A.; Sadrzadeh, M. Green Electrospun Membranes Based on Chitosan/Amino-Functionalized Nanoclay Composite Fibers for Cationic Dye Removal: Synthesis and Kinetic Studies. *ACS Omega* **2021**, *6*, 10816−10827.